Frequency-Dependent *Escherichia coli* Chemotaxis Behavior

Xuejun Zhu,[1,2] Guangwei Si,[1,2] Nianpei Deng,[2] Qi Ouyang,[1,2] Tailin Wu,[2] Zhuoran He,[2] Lili Jiang,[3]
Chunxiong Luo,[1,2,*] and Yuhai Tu[2,4,†]

[1]*Center for Microfluidic and Nanotechnology, The State Key Laboratory for Artificial Microstructures and Mesoscopic Physics,
School of Physics, Peking University, Beijing, 100871, China*
[2]*Center for Theoretical Biology, Academy for Advanced Interdisciplinary Studies, Peking University, Beijing, 100871, China*
[3]*Laboratory for Functional Connectome and Development, Key Laboratory of Behavioural Science, Institute of Psychology,
Chinese Academy of Sciences, Beijing, 100101, China*
[4]*T. J. Watson Research Center, IBM, P.O. Box 218, Yorktown Heights, New York 10598, USA*
(Received 28 October 2011; published 23 March 2012)

We study *Escherichia coli* chemotaxis behavior in environments with spatially and temporally varying attractant sources by developing a unique microfluidic system. Our measurements reveal a frequency-dependent chemotaxis behavior. At low frequency, the *E. coli* population oscillates in synchrony with the attractant. In contrast, in fast-changing environments, the population response becomes smaller and out of phase with the attractant waveform. These observations are inconsistent with the well-known Keller-Segel chemotaxis equation. A new continuum model is proposed to describe the population level behavior of *E. coli* chemotaxis based on the underlying pathway dynamics. With the inclusion of a finite adaptation time and an attractant consumption rate, our model successfully explains the microfluidic experiments at different stimulus frequencies.

Cells use their signal transduction systems to transform physical or chemical stimuli to intracellular signals that eventually control gene expressions or enzyme activities in order to carry out the appropriate responses [1]. A well-studied example is the bacterial chemotaxis system that controls cell motility in response to external chemical cues enabling motile bacterial cells such as *E. coli* to migrate towards favorable conditions or to flee from repellents (see Refs. [2,3] for reviews). Much progress has been made in studying the bacterial chemotaxis signaling pathway [4–8]. Recently, the intracellular responses to various time-varying signals were measured quantitatively in immobilized cells [9], revealing the modular structure of the underlying signaling network and its dynamics [10]. However, it still remains a challenge to understand how the intracellular signaling dynamics determines the chemotaxis behavior of motile cells in natural environments that can vary both in space and time. We address this question in this Letter by using microfluidic experiments and developing a pathway-based population model. Previous microfluidic experiments have investigated chemotaxis behaviors in stationary spatial gradients [11–13]. Here, we develop a microfluidic system with periodically changing spatial gradients. Our experiments show that *E. coli* chemotaxis behavior depends strongly on the external driving frequency. These observations are inconsistent with the classical Keller-Segel (K-S) chemotaxis equation [14]. This discrepancy motivates us to develop a new pathway-based population model for chemotaxis, which shows good agreement with the experiments.

Our microfluidic device is shown in Fig. 1(a). It consists of two modulation parts and one observation channel. In each modulation part, the ratio of the injection speeds for buffer and attractant can be programmed to vary as a function of time, creating the desired time-varying composition of the solution mixture in the source channel. Details of the observation channel are shown in Fig. 1(b). The two narrow connection passes and part of the buffer regions at the side wall of the observation channel are filled with agarose gel. The hydrosol inside serves as a barrier to prevent bacteria from escaping and to stop unwanted flow caused by hydrodynamic pressure; meanwhile, it allows free diffusion of small attractant molecules. The two connection regions serve as two control points, where ligand concentrations can be precisely and independently controlled. The attractant concentration in the observation channel is determined by diffusion. When the attractant concentrations in the two source channels are tuned periodically with the same period but opposite phase, the concentration in the observation channel oscillates in time and appears quasilinear in space [see Fig. S2 in the Supplemental Material (SM) [15]].

We measured the (florescence-labeled) *E. coli* density in response to attractant wave with different periods $T = 80$, 100, 200, 400, 600, 800, and 1200 s. The bacterial density oscillates with the same period as that of the attractant (see movies S1 and S2 in SM [15]). However, the phase of the cell density oscillation relative to that of the attractant depends strongly on the driving frequency [Figs. 1(c) and 1(d)]. The full spatiotemporal cell density profiles for *L*-aspartate are shown in Fig. 2 for different *T*. The
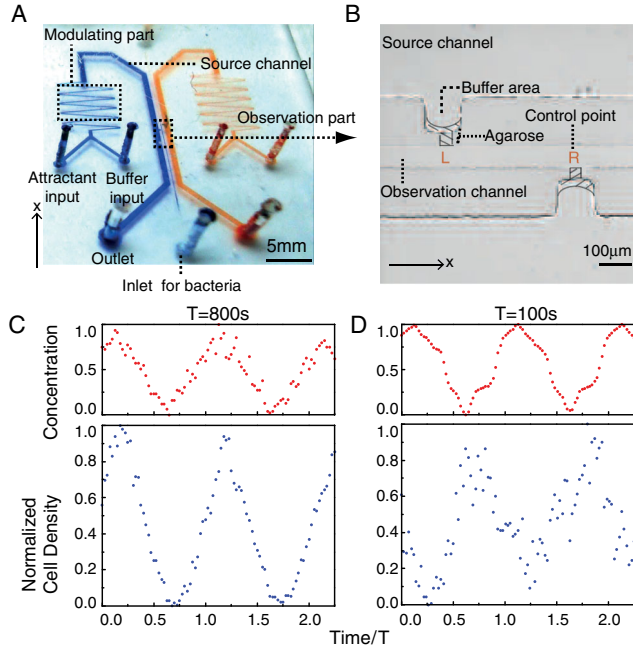
FIG. 1 (color online). Experimental setup. (a) A panoramic picture of the two-layer PDMS (polydimethylsiloxane) chip. (b) A zoomed-in view of the observation channel. The time lapse of the normalized *E. coli* density and attractant concentration at a control point is shown for periods $T = 800$ s (c) and 100 s (d). The ligand concentration is measured by adding a small amount of fluorescein into attractant stocks. Bacterial densities are determined by averaging the fluorescence intensity from the fluorescence-labeled cells in a region of $\pm 25\ \mu$m around the control points.
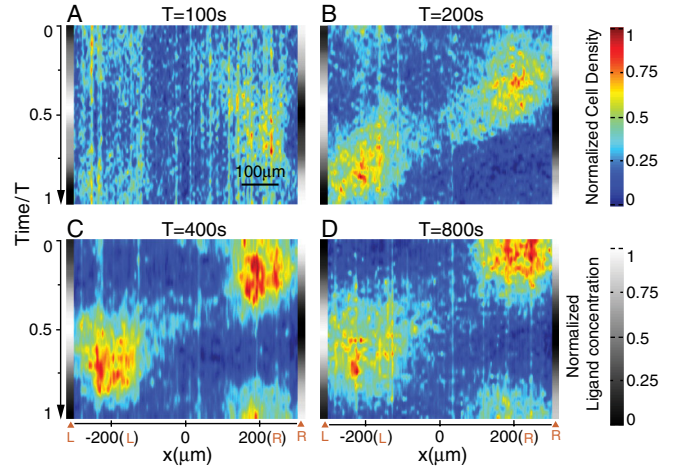

FIG. 2 (color online). The spatiotemporal profiles of the cell density for different driving periods. (a) $T = 100$ s, (b) $T = 200$ s, (c) $T = 400$ s, (d) $T = 800$ s. The normalized cell density at a given position x and time t (scaled by T) is represented by the color (see color bar). L-aspartate concentrations at the two source channels oscillate between 0.1 and 0.9 mM with opposite phases. The gray scale stripes at the two sides of each panel show the normalized ligand concentrations at the left (L) and right (R) control point as a function of time, $t = 0$ is when ligand concentration is maximum at the right control point. The cell density is measured 20 frames per period.

bacterial population inside the observation channel separates into two groups centered near the two control points. The migration of cells between the two groups is significant when the period is longer than 200 s [Figs. 2(b)–2(d)], and it is much reduced for higher driving frequencies [Fig. 2(a)]. Our experiments clearly show that for fast-varying gradients, the cell population cannot follow the attractant and exhibits oscillatory behaviors out of phase with the stimulus waveform, in contrast to its responses to slowly varying gradients.

The average motion of the bacterial population can be characterized by the center of mass (c.m.) of the bacteria within the observation window $[-300\ \mu$m, $300\ \mu$m$]$. In Fig. 3(a), we show the c.m. position versus time for different driving period T. Both the amplitude (A) of the c.m. and the phase difference ($\Delta\phi$) between the c.m. oscillation and the attractant oscillation change significantly with T. A increases with T and saturates when $T \geq 600$ s. Conversely, $\Delta\phi$ increases with decreasing T, from $(0.12 \pm 0.02)\pi$ at $T = 1200$ s to $(0.74 \pm 0.22)\pi$ at $T = 80$ s, as shown in Figs. 3(b) and 3(c).

Bacterial chemotaxis motion follows a run and tumble pattern with the tumbling frequency determined by the chemoeffector concentration and the chemoreceptor

methylation level, which is controlled by the adaptation process with a finite adaptation time τ. The cell's drift velocity v, determined by the bias of the tumbling frequency, should therefore also follow a relaxation dynamics (see SM [15] for a detailed derivation). To capture this relaxation dynamics of v in the simplest way possible, we use a Langevin equation where v follows a linear relaxation dynamics with a constant time τ:

$$\frac{dx}{dt} = v, \qquad \frac{dv}{dt} = -(v - v_d)/\tau + \eta, \qquad (1)$$

where v_d is the chemotaxis velocity. The Langevin equation is coarse grained in time beyond the average run time τ_r of individual cells; therefore, the fluctuation in velocity change $\eta(t)$ can be treated as a white noise: $\langle \eta(t)\eta(t')\rangle = 2\Delta\delta(t - t')$, with strength $\Delta = \Delta_0 v_0^2 \tau_r/\tau^2$, where Δ_0 is an order unity constant and v_0 is the average run speed. For simulations of chemotaxis motions of individual cells, we use the signaling pathway-based *E. coli* chemotaxis simulator (SPECS) model [16], where the internal signaling pathway dynamics is described by the interaction between the average receptor methylation level and the kinase activity which determines the switch probability of the flagellar motor and eventually the cell motion. According to the SPECS model simulations [16], the chemotaxis velocity can be approximately expressed as $v_d \approx C\frac{\partial G([L])}{\partial x}[1 + G_c^{-1}\frac{\partial G([L])}{\partial x}]^{-1}$, where $[L]$ is the ligand concentration and $G([L]) = \ln(1 + [L]/K_i) - \ln(1 + [L]/K_a)$ is the free-energy difference between active and inactive
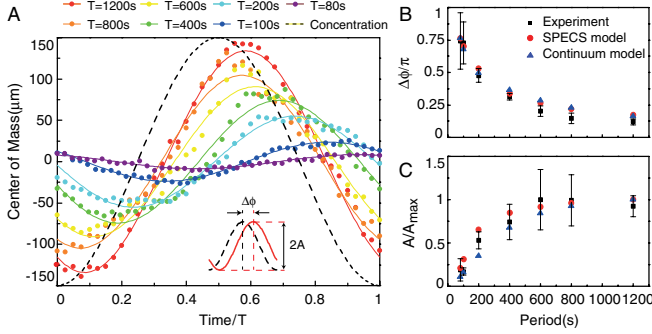
FIG. 3 (color online). Dynamics of the center of mass (c.m.). (a) The c.m. dynamics for different driving periods (T) are represented by dots of different colors, lines are fits to the data with a sinusoidal function $A\cos(2\pi t + \pi + \Delta\phi)$. The dotted black line shows the normalized ligand concentration at the right control point. (b) The phase shift $\Delta\phi$ and (c) the normalized amplitude $A/A_{\max}$ for different T are shown together with the model results. The error bars denote standard deviation of at least 4 repeats. Although A is small in high-frequency conditions (e.g., $T = 80$ s), it is still much larger than stochastic noise (see Fig. S9 in SM [15] for detail).

receptors, with dissociation constants K_a and K_i, respectively. The constants C and G_c depend on the biochemical parameters of the underlying pathway, such as receptor methylation/demethylation rates, receptor cluster size, and motor response cooperativity [16]. The parameters used here are $\tau = 35$ s, $\Delta = 0.75$ μm^2/s^3, $C = 8 \times 10^3$ μm^2/s, $G_c = 7 \times 10^{-4}$ μm^{-1}, $K_a = 3$ mM, $K_i = 18$ μM.

The probability distribution function of cells at position x with velocity v is given by $P(x, v, t)$. From the Langevin equation (1), we obtain the bivariate Fokker-Planck equation for $P(x, v, t)$:

$$\frac{\partial P(x, v, t)}{\partial t} = -\frac{\partial}{\partial x}(vP) + \tau^{-1}\frac{\partial}{\partial v}([v - v_d]P) + \Delta\frac{\partial^2}{\partial v^2}P,$$
(2)

which has the same form as the Kramers equation [17]. When all the relevant external time scales are much longer than the adaptation time τ, we can integrate out the v dependence by singular perturbation theory [18] (see SM [15] for details) or by approximating $P(x, v, t) \approx p(x, t)\delta(v - v_d)$ in Eq. (2) and derive the K-S equation:

$$\frac{\partial p(x, t)}{\partial t} \approx -\frac{\partial}{\partial x}(v_d p) + \Delta\tau^2\frac{\partial^2}{\partial x^2}p.$$
(3)

However, the K-S equation breaks down when external time scales become comparable to or shorter than τ.

The signal that a swimming cell encounters is determined by the time-varying external environment convoluted with its own biased random motion. Therefore, bacterial chemotaxis behaviors cannot be solely deduced from the signaling pathway dynamics of immobile cells

alone [9]. The population level chemotaxis model [Eq. (2)], which incorporates both the essential internal signaling dynamics [9] together with the cell motion, is needed to predict the population level chemotaxis behaviors in spatiotemporal varying environments. Equation (2) is solved (see SM [15] for details) to predict the chemotaxis behaviors in our experiments. As shown in Figs. 3(b) and 3(c), both the predicted amplitude and the phase shift of the c.m. are in quantitative agreement with the experiments as well as simulation results using SPECS [16].

The observed phase delay [Fig. 3(b)] may be partially attributed to the finite time needed for cell motion between the two control points. Simulations of the K-S equation [Eq. (3)] indeed show a finite phase shift in c.m. However, the phase shift from the K-S equation is much smaller than the experimental results for high-frequency stimuli (Fig. S3 [15]). The breakdown of the K-S equation is more pronounced at the control points where the effect of cell motion between the two control points is relatively small. As shown in Fig. 4, at the control point, the K-S equation would predict a small and roughly frequency-independent phase delay, which disagrees with our experiments. In our model [Eq. (2)] with finite adaptation time, the phase delay increases significantly with increasing frequency, in much better agreement with our experiments. The small difference between our current model and the experiments is probably due to the linearized relaxation dynamics used in Eq. (2). When more realistic nonlinear adaptation dynamics is used, such as in the SPECS model [16], the agreement with experiments becomes excellent (Fig. 4). We are currently working on improving our population model by incorporating more realistic internal adaptation dynamics.

Instead of only passively responding to their environment, cells can also change their own environment, e.g., by emitting or consuming attractant molecules [19]. We have investigated the effects of attractant consumption by using both the metabolizable attractant L-aspartate and its non-metabolizable analog α-methyl-DL-aspartate (MeAsp) in
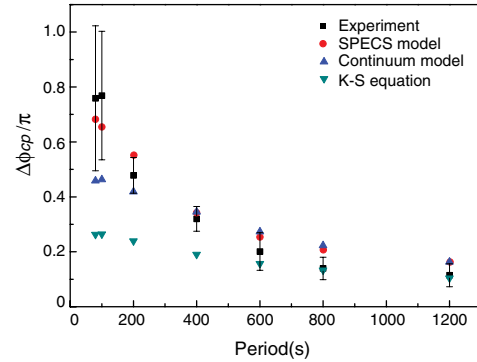

FIG. 4 (color online). The phase shift of the cell density oscillation at the control points ($\Delta\phi_{cp}$) as a function of the driving period from experiments and different models.
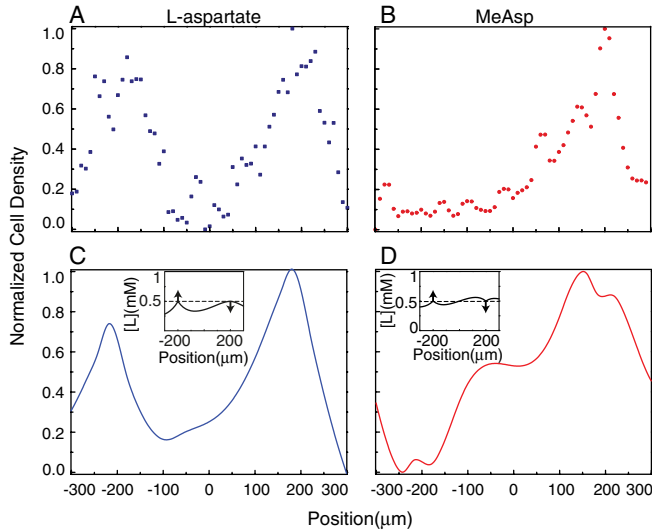
FIG. 5 (color online).   The comparison of (normalized) cell density profiles for (a) L-aspartate and (b) MeAsp at time $t = (n + 1/4)T$. There are two peaks for L-aspartate and one peak for MeAsp. The corresponding modeling results are shown in (c) for L-aspartate and (d) for MeAsp. The ligand concentration profiles and their trends at the control points are shown in the insets of (c) and (d). The period is $T = 80$ s.

our experiments. While the c.m. motion is qualitatively the same (see Fig. S4 [15] for MeAsp), we find the cell density profiles can be quite different for the two attractants. As shown in Figs. 5(a) and 5(b), at a particular time when the ligand concentrations, $[L]_L$ and $[L]_R$, at the left and right control points are equal but $[L]_L$ is increasing and $[L]_R$ is decreasing, the cell density profile peaks at both control points for L-aspartate, while it only peaks at the right control point for MeAsp.

Assuming the consumption rate depends linearly on the cell density, the ligand concentration follows:

$$\frac{\partial[L]}{\partial t} = D \frac{\partial^2[L]}{\partial x^2} - \frac{[L]}{\tau_c} \frac{n}{\langle n \rangle}, \tag{4}$$

where D is the diffusion coefficient of the ligand ($D \approx 500 \ \mu m^2/s$ used here), $n(x, t) = N_0 \int_{-\infty}^{\infty} P(x, v, t) dv$ stands for bacterial density (N_0 is the total number of bacteria in the channel), τ_c represents the consumption time at the mean density $\langle n \rangle$. By combining Eq. (4) with Eq. (2) and taking into account the different consumption rates for MeAsp ($\tau_c = \infty$) and L-aspartate ($\tau_c = 100$ s used here), the different cell density profiles can be reproduced [Figs. 5(c) and 5(d)]. This difference can also be understood intuitively. During the half period prevailing to the time point shown in Fig. 5, the ligand concentration at the right control point is higher than that of the left control point. For MeAsp, the ligand profile is only controlled by diffusion, and thus has a spatial gradient pointing towards the right control point between control points [Fig. 5(d), inset]. This spatial gradient drives the cell density to peak

only near the right control point. However, for L-aspartate, as the cells accumulate near the control points, the higher ligand consumption rates due to higher cell density there create local L-aspartate gradients towards both control points, which attracts more $E. coli$ cells. This positive feedback maintains the local high ligand concentration [Fig. 5(c), inset] and cell density peaks [Figs. 5(a) and 5(c)] at both control points against ligand and cell diffusions.

In summary, we have studied how $E. coli$ cells respond to spatiotemporal varying environments by developing a novel microfluidic device that can generate chemical gradients with a tunable frequency. We find that $E. coli$ chemotaxis response shows a significant phase delay when the external driving frequency becomes faster than the internal adaptation speed of the cells. Our measurements thus reveal a direct connection between the "microscopic" dynamics of the underlying signaling pathway and the "macroscopic" population level behaviors of the cells. This delay is also responsible for the "volcano" effect in bacterial distribution around a sharp attractant peak observed in computer simulations [20,21]. Motivated by these microfluidic experiments, we have developed a simple continuum model for bacterial chemotaxis wherein a finite relaxation time τ is introduced in the chemotaxis dynamics. We show that this new population model agrees well with the experiments even in the high-frequency regime where the classical K-S equation breaks down. Previous work [22] has considered the effect of the finite adaptation time by introducing the inertia term $\tau \partial^2 p/\partial t^2$ as a first order correction (in τ) to the K-S equation. Our bivariate model [Eq. (2)] is more accurate as it effectively keeps terms of all orders in τ. More importantly, new information on the signaling pathway dynamics, unknown when previous models were developed [14,22], has been used into our model, e.g., in the expression of the chemotaxis velocity v_d. The full nonlinear adaptation dynamics will be incorporated to further improve our population model.

*pkuluocx@pku.edu.cn
†yuhai@us.ibm.com.

[1] U. Alon, *An Introduction to Systems Biology: Design Principles of Biological Circuits* (Taylor & Francis, Boca Raton, FL, 2006), pp. 97–106.
[2] H. Berg, Phys. Today **53**, No. 1, 24 (2000).
[3] G. L. Hazelbauer, J. J. Falke, and J. S. Parkinson, Trends Biochem. Sci. **33**, 9 (2008).

[4] V. Sourjik and H. Berg, Proc. Natl. Acad. Sci. U.S.A. **99,** 123 (2002).

[5] T. Yi, Y. Huang, M. Simon, and J. Doyle, Proc. Natl. Acad. Sci. U.S.A. **97,** 4649 (2000).

[6] U. Alon, M. Surette, N. Barkai, and S. Leibler, Nature (London) **397,** 168 (1999).

[7] J. Keymer, R. Endres, M. Skoge, Y. Meir, and N. Wingreen, Proc. Natl. Acad. Sci. U.S.A. **103,** 1786 (2006).

[8] P. Cluzel, M. Surette, and S. Leibler, Science **287,** 1652 (2000).

[9] T. Shimizu, Y. Tu, and H. Berg, Mol. Syst. Biol. **6,** 382 (2010).

[10] Y. Tu, T. Shimizu, and H. Berg, Proc. Natl. Acad. Sci. U.S.A. **105,** 14 855 (2008).

[11] H. Mao, P. Cremer, and M. Manson, Proc. Natl. Acad. Sci. U.S.A. **100,** 5449 (2003).

[12] Y. Kalinin, L. Jiang, Y. Tu, and M. Wu, Biophys. J. **96,** 2439 (2009).

[13] T. Ahmed, T. Shimizu, and R. Stocker, Nano Lett. **10,** 3379 (2010).

[14] E. Keller and L. Segel, J. Theor. Biol. **30,** 225 (1971).

[15] See Supplemental Material at http://link.aps.org/supplemental/10.1103/PhysRevLett.108.128101 for details of gradient establishing, mathematical derivations, and a time-lapse movie.

[16] L. Jiang, Q. Ouyang, and Y. Tu, PLoS Comput. Biol. **6,** e1000735 (2010).

[17] H. Kramers, Physica (Amsterdam) **7,** 284 (1940).

[18] N. van Kampen, *Stochastic Processes in Physics and Chemistry* (North Holland, Amsterdam, 1992).

[19] E. O. Budrene and H. C. Berg, Nature (London) **349,** 630 (1991).

[20] D. Bray, M. Levin, and K. Lipkow, Curr. Biol. **17,** 12 (2007).

[21] J. Simons and P. Milewski, Math. Comput. Modell. **53,** 1374 (2011).

[22] R. Erban and H. Othmer, SIAM J. Appl. Math. **65,** 361 (2004).